Large-scale volcanic deposit fluidization by dilute pyroclastic density currents

Karim Kelfoun, Antonio Proaño

Large–scale volcanic deposit fluidisation by dilute pyroclastic density currents

Published in **Nature Geoscience, 2023**

DOI - https://doi.org/10.1038/s41561-023-01190-7

Karim Kelfoun[1], Antonio Proaño[1,2]

1. Université Clermont Auvergne, CNRS, IRD, OPGC, Laboratoire Magmas et Volcans, F-63000 Clermont-Ferrand, France. Corresponding author: karim.kelfoun@uca.fr
2. Instituto de Investigación Geológico y Energético (IIGE), Quito 170503, Ecuador

Introductory paragraph

There is increasing evidence that fine-grained deposits of pyroclastic density currents can be remobilized on a large scale, resulting in concentrated flows. These flows can be a major hazard: for example, at Soufrière Hills Volcano (Montserrat) in 1997, some travelled beyond the designated danger zone to inhabited areas. Despite their hazard potential, the scale and generation mechanism of these flows are poorly understood. Here we demonstrate using laboratory experiments and numerical modelling that decompression following the passage of dilute pyroclastic density currents can cause rapid deposit fluidization over areas of several square kilometres and to depths of tens of centimetres. The fluidized volume can be substantially greater than that deposited by the triggering pyroclastic density current because of remobilization of previously emplaced deposits, and the fluidized volume can flow even on slopes of a few degrees. The capacity for remobilization of a deposit is limited by its particle cohesion, which rapidly increases with atmospheric humidity. This mechanism of fluidisation should alert us to an under-appreciated volcanic hazard of long–runout pyroclastic flows that can be generated by remobilisation very rapidly and with little warning.

Main

Ground–hugging pyroclastic density currents (PDCs) are made up of a mixture of gas and volcanic particles. They cover a broad spectrum of densities from dilute to concentrated. Dilute currents, also called nuées ardentes and pyroclastic surges[1–3], transport particles predominantly by turbulent suspension[4]. These currents may originate at an eruptive vent or as the turbulent cloud atop a concentrated PDC. Their particle concentrations are relatively low ($< 5\%$[5–7]) except close to the ground, where they increase[2] and where particles are deposited through bed–load mechanisms (such as saltation, traction and rolling)[3]. Dilute PDCs easily escape any valley topography to cover the interfluves over large areas (several km²)[8–11].

Field evidence such as slumps, overturned deposit laminations and block sag structures (ref[12] and therein) show that the deposits formed by dilute PDCs can experience a fluid behaviour locally. The deposits can be in such a fluid state that coarse ash grains falling onto them forms tiny sag structures[13]. At a much larger scale, the fluidity could affect extensive areas, up to several hundred square metres, and, on slopes, the remobilized deposit could evolve into a concentrated flow able to move hundreds to thousands of metres independent of the parent dilute PDC. This phenomenon, called surge–derived pyroclastic flow, was observed particularly well at Montserrat in 1997[14,15], and where also documented at Mount St Helens[16,17], Montagne Pelée[18], Merapi[11] and at phreatomagmatic Ubehebe Crater[12,13,19]. Among the various mechanisms evoked for localised fluidisation (ref[12] and therein), the role of pore gases is thought to be highly influential. Field evidence, such as segregation pipes and surface craters, indicate gas defluidisation after emplacement[3,11,16,20]. The current explanation for large–scale remobilisation is that gases are trapped during rapid sedimentation of the dilute PDC[13,15]. As with the dramatic large–scale liquefaction by water[21–27], the pressure gradient between the pressurized interior of the deposit and the surface could counterbalance the weight of the particles[28–34]. The normal stress between the particles drops and, consequently, the resisting shear stress decreases too. If the pressure gradient is steep enough, then the deposit behaves as a fluid and, especially on steep slopes, can begin to flow. However, it is not clear how such an overpressure builds up. Indeed, while a densely–packed deposit of fine particles can retain gases[32,35], the spaces between the particles probably allow the gas to escape when the particles settle out of the dilute PDC except at very high settling rates[34,36] that seem incompatible with their runouts and the mass of particles transported.

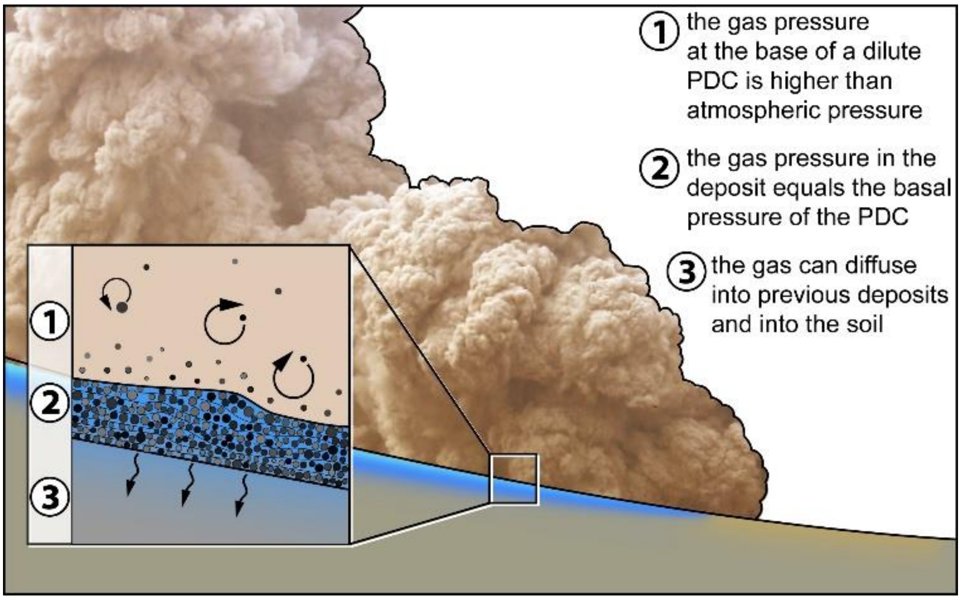

Figure 1. Emplacement of a dilute PDC**.** (a) The pressure of the gas, at its base, is higher than atmospheric pressure. Consequently, it is higher in the resulting deposit. This induces deposit fluidisation in the aftermath of the PDC, when the surface pressure drops back down rapidly enough.

One characteristic of dilute PDCs has not been studied up to now: due to their depth, density and velocity, the gas pressure at their base is higher than atmospheric pressure. The pressure of the interstitial gas in the deposits they form is thus also higher (Fig 1). After the passage of a PDC, the pressure of the gas at the surface must drop back to atmospheric pressure. A gas pressure gradient is thus temporarily created between the interior of the deposit and its surface. Is this pressure gradient enough to fluidise the deposit? What might the consequences of this type of fluidisation be?

To answer these questions, we designed an experimental pressurized tank (see Methods) filled with granular material (Fig 2). Pressure sensors in the granular bed measure the air pressure at different depths. To ensure that the observed phenomena reproduce conditions that could also occur in the field, the experiment setup has been scaled to nature in term of overpressure, deposit thickness and particle permeability. We also developed a numerical model to further explore the larger range of parameters found in actual volcanic fields.

Range of parameters studied

Particles deposited by dilute PDCs typically ranges from tens of microns to a few millimetres[11,20,37]. The gas permeability K, related to the particle size, can be as low as 10^{-13}–5×10^{-12} m² in ignimbrite and pumice deposits[35,38]. For deposits of dilute PDC and surge–derived pyroclastic flows, K has been estimated between 10^{-11} and 10^{-10} m² although the finest particles found in these deposits (< 20 μm) can significantly lower this value[11,20,38,39]. Dilute PDC deposits is typically of some centimetres to tens of centimetres thick[11,19,20]. Because they may overlie previous deposits into which the gas can diffuse, we have explored deposit thicknesses H of up to 10 m. We have also explored a large range of deposit densities ρ, between 500 to 2000 kg/m^3. The air viscosity is between $\mu = 1.85\times10^{-5}$ (at 20°C) and 4.5×10^{-5} Pa s (at 950°C).

The maximal static gas pressure at the base of a moderate PDC and its unloading time (i.e. the time to drop back from the maximal static pressure to atmospheric pressure) can be estimated indirectly through numerical simulations of PDC emplacement at Merapi[40] and Montserrat[41] at 5–10 kPa and 5–30 s, respectively. However, the total gas pressure at the base of a PDC must also include the dynamic pressure which depends on the PDC density ρ_s and its velocity u_s, and is given by $\frac{1}{2}\rho_s u_s^2$. The maximal particle concentration carried by turbulence in a dilute PDC is about 5% vol.[5–7] i.e. a density of about ρ_s = 70 kg/m^3. With a velocity of 40 m/s[42,43], the dynamic pressure increases by more than 50 kPa at certain places where the current meets rises in topography. Moreover, turbulence can create fluctuations in pressure of up to three times that of the mean dynamic pressure[44]. These pressure fluctuations can also cause higher than expected unloading rates. To take these uncertainties into account, we have explored a large range of initial basal pressures P_{s0} (1–100 kPa) over the atmospheric pressure (P_{atm}), a large range of unloading times Δt (0–300 s) and, consequently, a large range of unloading rates (10 Pa/s to >20 kPa/s).

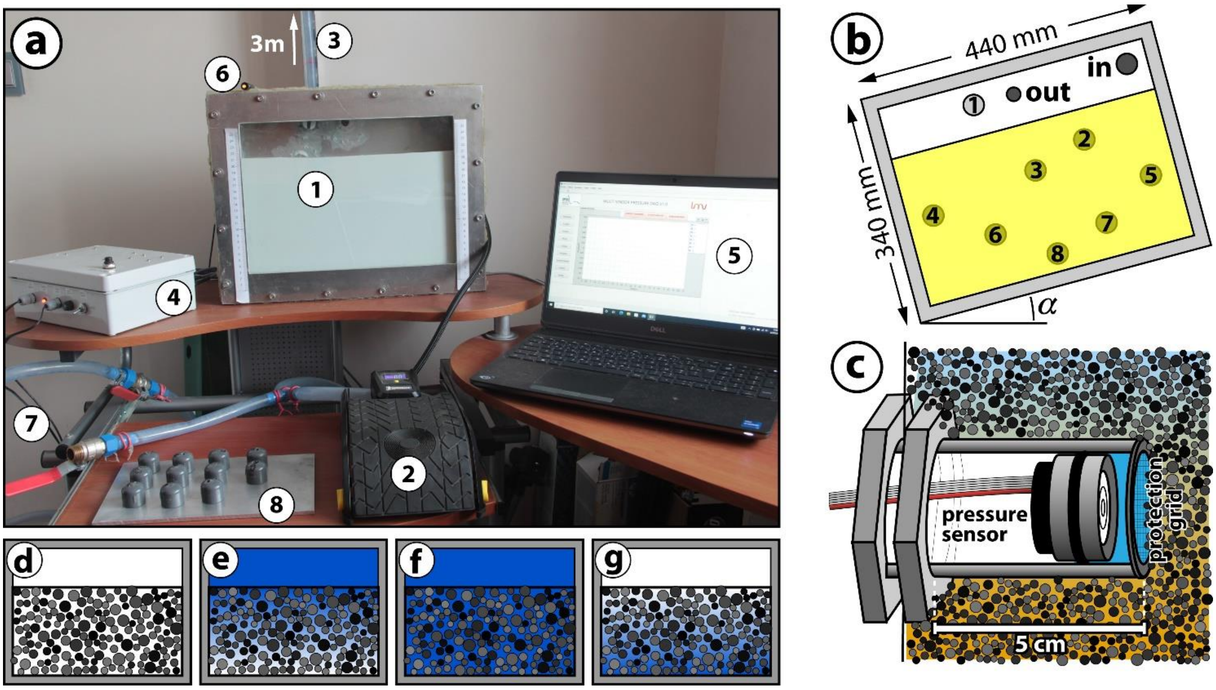

Figure 2: The experimental device made to simulate the unloading of a dilute PDC. (a) (1) the sealed tank partially filled with granular material, (2) pump, (3) vertical pipe filled with water for sensor calibration, (4) acquisition device, (5) computer and our dedicated acquisition software, (6) LED for synchronisation of videos and pressure measurements, (7) depressurisation valve, (8) pierced caps. (b) Locations of the pressure sensors, numbered 1–8. (c) Schematic representation of one of the sensors used to measure the gas pressure at various depths in the granular bed (located on 2b). (d) Initially, the air between the particles and that above is at atmospheric pressure. (e) The air is then pressurised (using a pump (2) in (2a) and diffuses between the particles. (f) When the pressure is equalized, the valve (7) in (2a) is opened. A cap (8) in (2a) screwed on to the valve controls the decompression rate. Decompression is slower between the particles than above them. (g) This creates a pressure gradient that can fluidise the particle bed.

Experimental results

The experimental procedure is described in the Methods section. The air is first pressurized above the granular material, leading to a gas pressure increase between the particles. After the valve is opened, the pressure of the air above the granular bed drops (Fig. 2d–g and Fig. 3). The pressure of the air in the bed itself drops in turn, but with a time delay that depends on the bed's permeability, its total thickness and on the distance to the bed surface. The difference between the pressure within the bed and at its surface increases rapidly (Fig. 3b), creating a gas pressure gradient that can counterbalance the weight of the particles. For low decompression rates (e.g. < 2 kPa/s, see how this value is calculated in Methods), the gas pressure drops in the bed but no movement of the granular material is detected. For intermediate decompression rates (between 2 kPa/s and 8 kPa/s, Fig. 4a), the decompression causes an expansion of the granular material. Experiments with different slope angles show granular flow occurring even on a slope of a few degrees, which indicates partial fluidisation of the granular material. Bubbles can be observed in the bed. For high decompression rates (>8 kPa), the granular material exhibits very fluid behaviour: it flows even on very gentle initial slopes (5°) and forms waves that oscillate before coming to a standstill on a nearly horizontal surface (Fig. 3c). Bubbles, whose size increases with the decompression rate, form in the granular bed and burst at its surface (Fig. 3f–g) forming degassing craters.

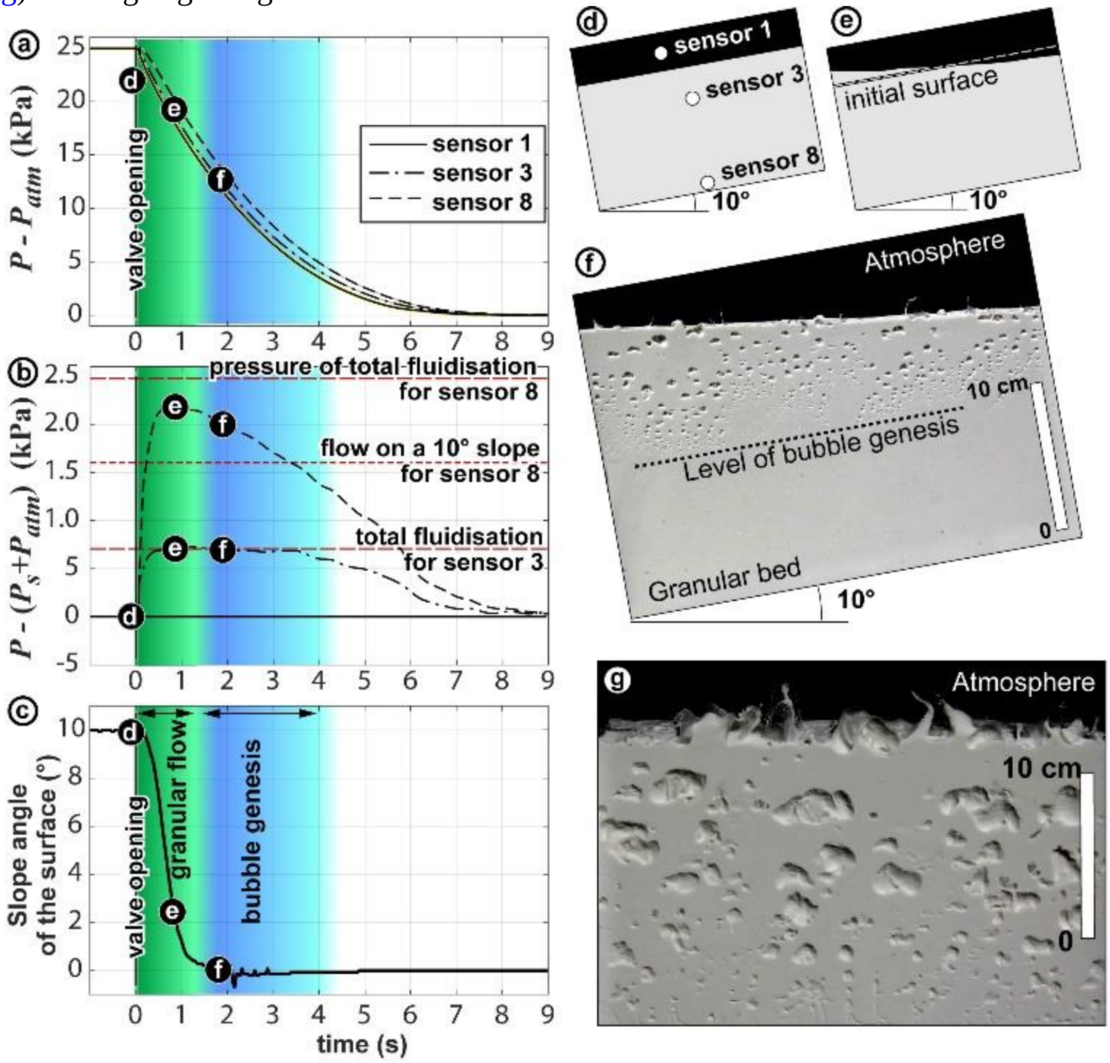

Figure 3: Results of the decompression experiments. (a) Evolution of the pressure with an initial slope of 10° (d, e and f), an initial overpressure P_{s0} of 25 kPa and a maximal decompression rate of ~11 kPa/s (mean 5 kPa/s) for the three sensors shown in (d). The letters in the black circles refer to the locations of figures d–g. (b) Gas pressure difference between sensors 3 and 8, and the granular bed surface (sensor 1). The horizontal dashed lines show the pressure difference needed to fully fluidise the flows, or to enable flow on a 10° slope. (c) Evolution of the slope with time, from an initial angle of 10° to horizontal after fluidisation. (d) Initial geometry of the granular bed before decompression. (e) Flow of the granular bed before bubble genesis. (f) Bubble formation. The decompression rate makes that only the top half of the bed is able to fully fluidise (see caption (b)). (g) Full fluidisation of the whole granular bed and high bubble formation at lower initial pressure (17 kPa) but with a higher decompression rate (79 kPa/s).

Movies of some experiments synchronized with pressure data are given in Data availability. Similar results have been obtained using natural material at high temperature (>100°C). However, below 100°C, the natural material is very sensitive to temperature, probably due to interaction with air humidity, and cohesive behaviour can be observed: cracks form during decompression that coalesce to form preferential paths by which the gas escapes, carrying with it the smallest particles and forming fine–depleted degassing pipes while reducing the effectiveness of fluidisation.

Numerical simulation of the fluidisation

To explore the whole ranges of unloading (i.e. decompression) conditions (P_{s0}, Δt, μ) and of deposit characteristics (K, H, ρ) defined in the section *Range of parameters studied*, we have written a numerical model for defluidisation (downloadable in Code availability) inspired by the work of ref[35]. We have validated the numerical model against our experimental results in terms of the evolution of the pressure with time and the capacity of the granular bed to flow on a slope. Then we have used the model to explore a broader range of conditions (see Methods and Extended Data Fig. 1).

Analysis of the numerical results shows that the system is controlled by two dimensionless numbers. $\Pi_1 = \dfrac{\rho g H}{P_{s0}}$ controls the maximal depth of fluidisation with respect to the PDC pressure, with g as gravity. $\Pi_2 = \dfrac{H^2 \mu}{K \bar{P}_s \Delta t}$ is a ratio of the characteristic defluidisation time of the granular bed over the unloading time Δt of the dilute PDC, with $\bar{P}_s$ the mean value of gas pressure during unloading approximated by $\bar{P}_s = P_{atm} + P_{s0}/2$ (see Methods).

The maximal gradient of the gas pressure is systematically at the surface of the granular bed and this explains why the fluidisation (number of bubbles and granular flow) is higher at the surface of our experiments than at the bottom. We use the term 'full fluidisation' where the pressure gradient of the gas equals that of the particles and where, consequently, friction between the particles is zero. Full fluidisation can affect the entire bed or the upper part alone. Fig 4a (and Extended Data Fig. 2) shows the ratio H_f / H of the fully fluidised depth, H_f, (from the surface) over the total bed thickness, H, according to Π_1 and Π_2. $\Pi_1 = 1$ is the limit for the full fluidisation of the entire bed and, at higher values (thicker deposits or lower pressures), the upper part of the granular material alone is fluidised.

A thin or very permeable deposit loses its gas rapidly (dark grey domain, Fig. 4a) while a thick or low permeability deposit (light grey and white domains) retains the gas longer, maintaining the pressure difference needed for full fluidisation of its upper part. Analysis of Π_1 and Π_2 shows that low permeability deposits ($K = 10^{-12}$ m²) are fluidised relatively easily except at low thicknesses (<10 cm) or over long unloading times. For example, with P_{s0} =10 kPa, ρ = 1500 kg/m^3 and $\mu = 3\times10^{-5}$ Pa s, a deposit of 20.4 cm, 68 cm and 4 m experiences full fluidisation at its surface for unloading times, Δt, of less than 23s, 76s and 234 s respectively (Fig. 4a, point α: Π_1=0.3 and Π_2=0.5, point β: Π_1=1 and Π_2=1.7, point γ: Π_1=6 and Π_2=20). For Π_1=0.3, the deposit is entirely fluidised for Π_2>2, i.e. for Δt<5.8s. Figure 4a also gives the values of $t_{f10}/\Delta t$, the ratio of t_{f10} (the period of full fluidisation of the upper 10 centimetres of the granular bed, Fig. 4c), over the unloading time. In extreme cases, the bed can remain fluidised for several minutes after the passage of the dilute PDC. For example, with H=5m, ρ=1000 kg/m^3 and P_{s0} = 50kPa, Π_1 = 0.98 (point ε). With $K=10^{-12}$ m² and Δt=120 s, Π_2 = 49.5. The deposit is thus fluidised over nearly its whole thickness and $t_{f10}/\Delta t \approx 8$ indicates that the upper 10 centimetres are fluidised for more than 15 minutes by gas escaping from below.

The higher permeabilities (K = 10^{-11} m^2) require thicker deposits, higher pressures or shorter unloading times to achieve fluidisation, but a significant depth of material can become fully fluidised. For example, with P_{s0} = 50 kPa , Δt = 60 s and ρ=1500 kg/m^3 (Fig. 4b–c), 35% of the deposit is fully fluidised (i.e. down to a depth of 1.75 m) for a deposit thickness of 5 m (point ζ: Π_1 = 1.47, Π_2 = 9.90). The upper 10 centimetres are fully fluidised for about 40 s ($t_{f10}/\Delta t$ ≈66%). Finally, it should be noted that full fluidisation is not required to initiate a flow. For the previous example (H = 5m, P_{s0} = 50 kPa, Δt = 60 s), the upper 10 cm can flow for 80 s on a 10° slope and 80% of the deposit thickness (i.e. 4 m) can be remobilized (φ = 10°, white line Fig. 4c, see Methods for explanation of the apparent friction angle φ). The prediction of the deposit thickness that can flow on a given slope is predicted by a shift in the curves (white curves, Fig 4a).

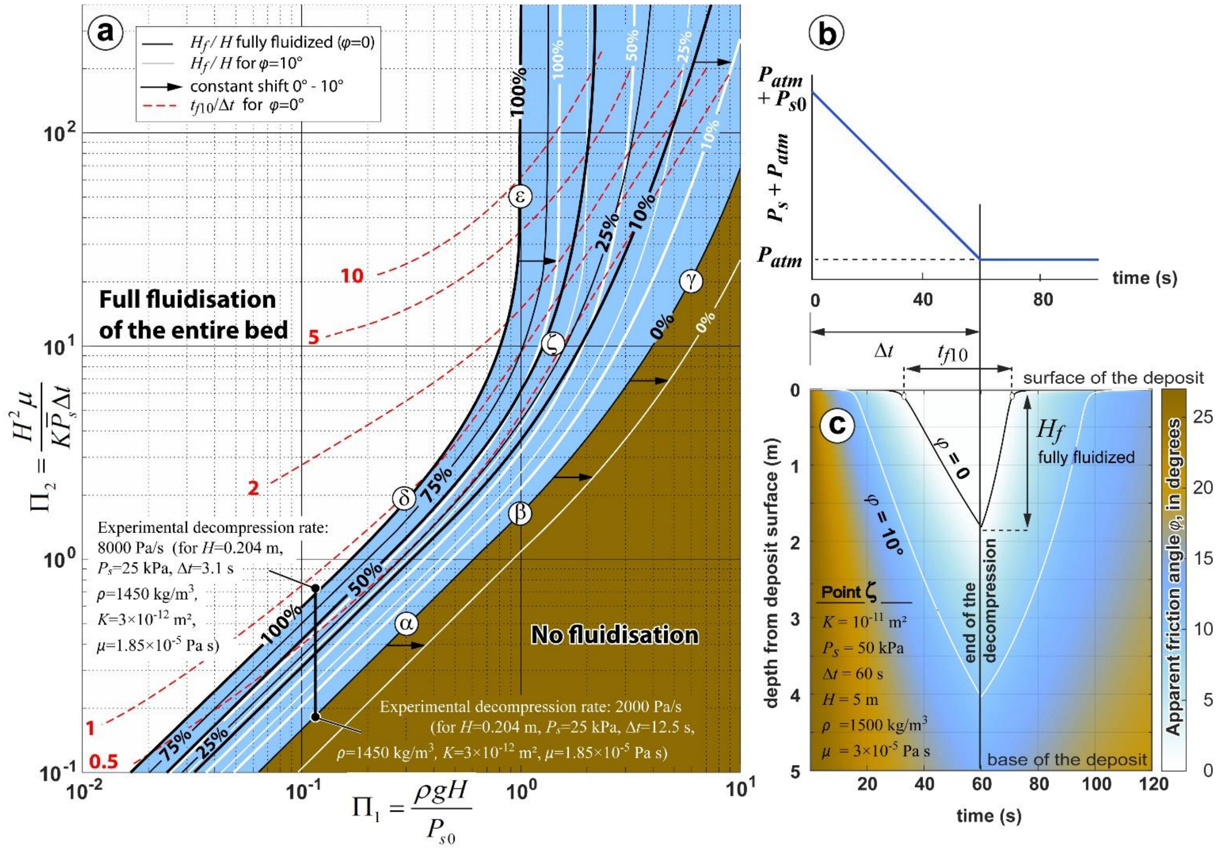

Figure 4: Results of the numerical study of the fluidisation by the unloading of a dilute PDC. (a) Evolution of the ratio H_f/H using to Π_1 and Π_2. The black curves give the values of H_f/H for a full fluidisation (φ=0°). The white curves, which are slightly shifted black curves, give H_f/H that flow on a 10° slope (φ=10°). The dashed curves give the value of $t_{f10}/\Delta t$. Greek letters refer to explanations in the text. The two experimental decompression rates used as examples in the text are also reported (Π_1 = 0.116). (b) Evolution of the gas pressure imposed at the surface of the deposit for point ζ. (c) Evolution of the friction angle of the deposit with time for P_{s0}=50 kPa, K=10^{-11} m^2 and Δt=60 s (point ζ). Total fluidisation (φ = 0) affects a depth of 1.75 m and the upper part of the deposit is fluidised for 40 s. Material can flow down slopes greater than 10° to a maximal depth of 4 m and the upper 10–cm can flow over this slope for about 80 s.

Implications of large–scale fluidisation

The capacity of a dilute PDC to trigger remobilisation of the underlying deposits is mainly related to the permeability of the deposit and, consequently, the size of its particles[38,45]. We show that for a permeability of 10^{-12} m² or less, realistic conditions of dilute PDC unloading and deposit thickness are compatible with deposit fluidisation and resulting concentrated flow on a slope. For a permeability of more than 10^{-11} m^2, full fluidisation only occurs at the surface of thick deposits (>1 m). Are these conditions realistic for volcanic environments? Deposits in nature are rarely emplaced onto an impermeable basement and instead tend to be emplaced onto volcaniclastic deposits from previous activity (ash fall or PDC deposits). When the dilute PDC flows over such deposits, its pressure diffuses down into them, and they can exhibit the behaviour described above after the unloading due to the passage of the current. Thus, 10, 20 or 50 cm of a deposit can be totally fluidised for a period of tens of seconds if a dilute PDC moves over a thick sequence of previous permeable deposits.

We conclude that deposit fluidisation by dilute PDC unloading could be a relatively common phenomenon. We think that it was the cause of the concentrated surge–derived pyroclastic flows observed at Montserrat in 1997[14,15] and our model is fully compatible with the 'ash boiling' described[15]. It is also compatible with observations at Ubehebe Crater[13,19] and particularly the conclusion that the deposit was inflated and soft shortly after deposition[19]. The fact that surge–derived pyroclastic flows are not very commonly described in the literature is probably due to the difficulty of identifying them, since the topography generally causes these secondary concentrated flows to move into channel bottoms and blend with primary concentrated flows in process, making it difficult to distinguish between the two. Our study proposes a new physical framework for the interpretation of this kind of deposits. Note that our mechanism is still compatible with local preservation of the sedimentary structures (dune, lamination, etc.) observed in the field: it affects the deposit after deposition and only where the unloading conditions are compatible with fluidisation.

The capacity for remobilization by the new mechanism revealed by our study is limited by particle cohesion, which is rapidly increased by rain or atmospheric humidity. In these conditions, the gas escapes through fractures, limiting the possibility for particles to flow, as shown in the low temperature ignimbrite experiments. Thus, it seems unlikely that a PDC could remobilize very large volumes of soil or old volcanic deposits. However, during an eruptive phase, the particles might not be affected by atmospheric humidity. Each dilute PDC can pass over several square kilometres of deposit[8,9,11,20,40,41]. If thicker, denser or faster–moving PDC develops, fluidisation conditions can be reached. Huge volumes of material accumulated over large areas during a period of a number of days could suddenly be remobilized over an area of several square kilometres. Thick concentrated flows of fine particles could then be generated across the whole area covered by the dilute PDC and could reach long distances with little warning on volcanic slopes, destroying areas previously considered to be safe. Volcanic phenomena are complex and unknown mechanisms clearly pose a challenge for hazard assessment. Our study shows that a dilute PDC can mobilize significantly more material than it has deposited. This new hazard and the associated risks must be taken into account for future estimates of volcanic threats.

Acknowledgements

This is contribution no. 590 of the ClerVolc program of the International Research Center for Disaster Sciences and Sustainable Development of the University Clermont Auvergne. We thank Thierry Latchimy, Edouard Régis, Eric Brut, Jean-Louis Fruquière and Cyrille Guillot for their help in the construction of the experimental devices. The comments of Pr. Greg Valentine contributed significantly to the improvement of the article.

Author contributions

Conceptualization: K.K. Laboratory experiments: K.K. & A.P. Numerical code: K.K. Writing—original draft: K.K. & A.P. Writing—review and editing: K.K. Funding acquisition: K.K.

Competing interests Statement

The authors declare that they have no known competing financial interests or personal relationships that have influenced the work reported.

Figure captions

Figure 1. Emplacement of a dilute PDC**.** (a) The pressure of the gas, at its base, is higher than atmospheric pressure. Consequently, it is higher in the resulting deposit. This induces deposit fluidisation in the aftermath of the PDC, when the surface pressure drops back down rapidly enough.

Figure 2: The experimental device made to simulate the unloading of a dilute PDC. (a) (1) the sealed tank partially filled with granular material, (2) pump, (3) vertical pipe filled with water for sensor calibration, (4) acquisition device, (5) computer and our dedicated acquisition software, (6) LED for synchronisation of videos and pressure measurements, (7) depressurisation valve, (8) pierced caps. (b) Locations of the pressure sensors, numbered 1–8. (c) Schematic representation of one of the sensors used to measure the gas pressure at various depths in the granular bed (located on 2b). (d) Initially, the air between the particles and that above is at atmospheric pressure. (e) The air is then pressurised (using a pump (2) in (2a) and diffuses between the particles. (f) When the pressure is equalized, the valve (7) in (2a) is opened. A cap (8) in (2a) screwed on to the valve controls the decompression rate. Decompression is slower between the particles than above them. (g) This creates a pressure gradient that can fluidise the particle bed.

Figure 3: Results of the decompression experiments. (a) Evolution of the pressure with an initial slope of 10° (d, e and f), an initial overpressure P_{s0} of 25 kPa and a maximal decompression rate of ~11 kPa/s (mean 5 kPa/s) for the three sensors shown in (d). The letters in the black circles refer to the locations of figures d–g. (b) Gas pressure difference between sensors 3 and 8, and the granular bed surface (sensor 1). The horizontal dashed lines show the pressure difference needed to fully fluidise the flows, or to enable flow on a 10° slope. (c) Evolution of the slope with time, from an initial angle of 10° to horizontal after fluidisation. (d) Initial geometry of the granular bed before decompression. (e) Flow of the granular bed before bubble genesis. (f) Bubble formation. The decompression rate makes that only the top half of the bed is able to fully fluidise (see caption (b)). (g) Full fluidisation of the whole granular bed and high bubble formation at lower initial pressure (17 kPa) but with a higher decompression rate (79 kPa/s).

Figure 4: Results of the numerical study of the fluidisation by the unloading of a dilute PDC. (a) Evolution of the ratio H_f/H using to Π_1 and Π_2. The black curves give the values of H_f/H for a full fluidisation (φ=0°). The white curves, which are slightly shifted black curves, give H_f/H that flow on a 10° slope (φ=10°). The dashed curves give the value of $t_{f10}/\Delta t$. Greek letters refer to explanations in the text. The two experimental decompression rates used as examples in the text are also reported (Π_1 = 0.116). (b) Evolution of the gas pressure imposed at the surface of the deposit for point ζ. (c) Evolution of the friction angle of the deposit with time for P_{s0}=50 kPa, K=10^{-11} m^2 and Δt=60 s (point ζ). Total fluidisation (φ = 0) affects a depth

of 1.75 m and the upper part of the deposit is fluidised for 40 s. Material can flow down slopes greater than 10° to a maximal depth of 4 m and the upper 10–cm can flow over this slope for about 80 s.

References

1. Sparks, R. S. J. & Walker, G. P. L. The ground surge deposit: a third type of pyroclastic rock. *Nat. Phys. Sci.* 241(107), 62–64 (1973).
2. Valentine, G. A. Stratified flow in pyroclastic surges. *Bull. Volcanol.* 49(4), 616–630 (1987).
3. Branney, M. & Kokelaar, P. *Pyroclastic Density Currents and the Sedimentation of Ignimbrites* Geological Society Memoir No. 27 (Geological Society, London, 2002).
4. Dufek, J., Esposti Ongaro, T. & Roche, O. Pyroclastic density currents: processes and models. Chapter 35. Part IV Explosive Volcanism, The Encyclopedia of Volcanoes (2015).
5. Andrews, B. J. & Manga, M. Experimental study of turbulence, sedimentation, and coignimbrite mass partitioning in dilute pyroclastic density currents. *J. Volcanol. Geoth. Res.* 225, 30–44 (2012).
6. Breard, E. C. P., Lube, G., Jones, J. R., Dufek, J., Cronin, S. J., Valentine, G. A., & Moebis, A. Coupling of turbulent and non–turbulent flow regimes within pyroclastic density currents. *Nat. Geosci.*, 9(10), 767–771 (2016).
7. Weit, A., Roche, O., Dubois, T., & Manga, M. Maximum solid phase concentration in geophysical turbulent gas-particle flows: Insights from laboratory experiments. *Geophys. Res. Lett.*, 46, 6388–6396 (2019).
8. Yamamoto, T., Takarada, S. & Shigeru S. Pyroclastic flows from the 1991 eruption of Unzen volcano, Japan. *Bull. Volcanol.* 55, 166–175 (1993).
9. Cole, P. D. & al. Deposits from dome-collapse and fountain-collapse pyroclastic flows at Soufriere Hills Volcano. Montserrat. In: Druitt, T. H. & Kokelaar, B. P. (eds) The Eruption of Soufriere Hills Volcano, Montserrat, from 1995 to 1999. *Geological Society, London. Memoirs*, 21, 231–262 (2002).
10. Bourdier, J. L., Boudon, G., & Gourgaud, A. Stratigraphy of the 1920 and 1929 nuée-ardente deposits. Mt. Pelée, Martinique. *J. Volcanol. Geotherm. Res.* 38, 77–96 (1989).
11. Komorowski, J. C. & al. Paroxysmal dome explosion during the Merapi 2010 eruption: Processes and facies relationships of associated high-energy pyroclastic density currents. *J. Volcanol. Geotherm. Res.* 261, 260–294 (2013).
12. Douillet, G. A. & al. Syn- eruptive, softsediment deformation of deposits from dilute pyroclastic density current: Triggers from granular shear, dynamic pore pressure, ballistic impacts and shock waves. *Solid Earth*, 6, 553–572 (2015).
13. Valentine, G. A., Fierstein, J. & White, J.D.L. Pyroclastic deposits of Ubehebe Crater, Death Valley, California, USA: Ballistics, pyroclastic surges, and dry granular flows. *Geosphere*. 18 (6) 1926– 1957 (2022).
14. Calder, E. S. & al. Mechanisms of lava dome instability and generation of rockfalls and pyroclastic flows at Soufriere Hills Volcano, Montserrat. In: Druitt, T.H. & Kokelaar, B.P. (eds) The Eruption of Soufriere Hills Volcano, Montserrat, from 1995 to 1999. *Geological Society, London, Memoirs*, 21. 173–190 (2002).
15. Druitt, T. H. & al. Small-volume, highly mobile pyroclastic flows formed by rapid sedimentation from pyroclastic surges at Soufrière Hills Volcano, Montserrat: an important volcanic hazard. *Geological Society, London, Memoirs*, 21, 263–279 (2007).

16. Fisher, R. V. Transport and deposition of a pyroclastic surge across an area of high relief: the 18 May 1980 eruption of Mount St. Helens, Washington. *Geol. Soc. Am. Bull.*, 102(8), 1038–1054 (1990).
17. Hoblitt, R. P., Miller, D. C. & Vallance, J. E. Origin and stratigraphy of the deposits produced by the May 18 directed blast. In: Lipman, P.W. & Mullineaux, D.R. (eds) *The 1980 Eruptions of Mount St. Helens, Washington*. US Geological Survey, Professional Papers, 1250, 379–400 (1981).
18. Fisher, R. V., Smith, A. L. & Roobol, M. J. Destruction of St. Pierre, Martinique, by ash-cloud surges, May 8 and 20 1902. *Geology*. 8, 472-476 (1980).
19. Valentine, G. A., Fierstein, J. & White, J.D.L. Soft sediment deformation in dry pyroclastic deposits at Ubehebe Crater, Death Valley, California. *Geology*. 49, 211–215 (2021).
20. Ritchie L. J., Cole, P. D. & Sparks R. S. J. Sedimentology of deposits from the pyroclastic density current of 26 December 1997 at Soufrière Hills Volcano, Montserrat. *Geological Society, London, Memoirs*, 21, 435 – 456 (2015).
21. Cummins, P. R. Irrigation and the Palu landslides. *Nat. Geosci.* 12, 881–882 (2019).
22. Bradley, K. & al. Earthquake-triggered 2018 Palu Valley landslides enabled by wet rice cultivation. Nat. Geosci. 12, 935–939 (2019).
23. Watkinson, I. M. & Hall, R. Impact of communal irrigation on the 2018 Palu earthquake-triggered landslides. *Nat. Geosci.* 12, 940–945 (2019).
24. Massey, C. & al. Landslides triggered by the 14 november 2016 Mw 7.8 Kaik¯oura earthquake, New Zealand. *Bull Seismol, Soc Am.* 108(3B):1630–48 (2018).
25. Xu, C. & al. Landslides triggered by the 2016 Mj 7.3 Kumamoto, Japan, earthquake. *Landslides* 15(3): 551–64 (2018).
26. Ishihara, K. & Koga, Y. Case Studies of Liquefaction in the 1964 Niigata Earthquake. *Soils and Foundations*, 21(3), 35–52 (1981).
27. Yoshida, N. & al. Causes of Showa Bridge collapse in the 1964 Niigata earthquake based on eyewitness testimony. *Soils and Foundations*. 47 (6): 1075–1087 (2007).
28. Sparks, R. S. J. Particle size variations in ignimbrites and implications for the transport of pyroclastic flows. *Sedimentology*, 23:147–188 (1976).
29. Wilson, C. J. N. The role of fluidization in the emplacement of pyroclastic flows: an experimental approach. *J Volcanol Geotherm* Res 8:231–249 (1980).
30. Druitt, T. H. Pyroclastic density currents. *Geol. Society London Spec. Publ.* 145, 145–182 (1998).
31. Freundt, A. & Bursik, M. Pyroclastic flow transport mechanisms. In: Freundt A, Rosi M (eds) *From magma to tephra*. Elsevier, pp 173-245 (2001).
32. Roche, O. Depositional processes and gas pore pressure in pyroclastic flows: An experimental perspective. *Bull. Volcanol.* 74, 1807–1820 (2012).
33. Gueugneau, V., Kelfoun, K., Roche, O., & Chupin, L. Effects of pore pressure in pyroclastic flows: Numerical simulation and experimental validation. *Geophys. Res. Lett.*, 44, 2194– 2202 (2017).
34. Kelfoun, K. & Gueugneau, V. A unifying model for pyroclastic surge genesis and pyroclastic flow fluidization. *Geophys. Res. Lett.*, 49 (5) (2022).
35. Druitt, T. H., Avard, G., Bruni, G., Lettieri, P. & Maez, F. Gas retention in fine-grained pyroclastic flow materials at high temperatures. *Bull. Volcanol.* 69, 881–901 (2007).
36. Chedeville, C., & Roche, O. Autofluidization of collapsing bed of fine particles: Implications for the emplacement of pyroclastic flows. *J. Volcanol. Geotherm. Res.*, 368, 91– 99 (2018).
37. Walker, G. P. Grain-size characteristics of pyroclastic deposits. *J. Geol.*, 79(6), 696–714 (1971).

38. Breard, E. C. P. & al. The permeability of volcanic mixtures. Implications for pyroclastic currents. *J. Geophys. Res. Solid Earth*, 124 (2019).
39. Bareschino, P., et al. Fluidization and de-aeration of pyroclastic mixtures: The influence of fines content, polydispersity and shear flow. *J. Volcanol. Geotherm. Res.*, 164, (4), 284–292 (2007).
40. Kelfoun, K., & al. Simulation of block-and-ash flows and ash-cloud surges of the 2010 eruption of Merapi volcano with a two-layer model. *J. Geophys. Res.: Solid Earth*, 122 (6), 4277–4292, (2017).
41. Gueugneau, V., Kelfoun, K. & Druitt, T. H. Investigation of surge-derived pyroclastic flow formation by numerical modelling of the 25 June 1997 dome collapse at Soufrière Hills Volcano, Montserrat. *Bull. Volcanol.* 81 (2019).
42. Moore, J. G. & Rice, C. J. Chronology and character of the May 18, 1980, explosive eruptions of mount St Helens. In: *Explosive volcanism: inception, evolution and hazards*. National Academy Press, Washington, DC (1984).
43. Syarifuddin, M. & al. Estimating the velocity of pyroclastic density currents using an operational dual-PRF radar. *J. Volcanol. Geotherm. Res.*, 424 (2022).
44. Brosch, E., & al. Destructiveness of pyroclastic surges controlled by turbulent fluctuations. *Nat. Commun.* 12, 7306 (2021).
45. Geldart, D. (1973). Types of gas fluidisation. *Powder Technology*. 7(5), 285–292.

Methods

Experimental fluidisation by decompression

The experimental device is composed of an ~7 litre (length 40 cm, width 6 cm, height 30 cm) sealed tank partly filled with granular material (Fig 2a–b). Experiments were carried out with various thicknesses H (< 25 cm) of either particles from a natural deposit (ignimbrite from Neschers[35]) or glass beads with a granulometry close to the fine matrix of dilute PDC deposits (40–70 µm). The air pressure inside the tank could be raised (via the “in” hole, Fig 2b) up to P_{s0} = 30 kPa above atmospheric pressure (Fig. 2e–f). The pressurized air also pushed up a water column in a connected vertical pipe, providing an independent check on the pressure of the tank with an accuracy <10 Pa. A valve located above the granular material allowed the air to be decompressed to atmospheric pressure (“out” hole, Fig 2b). Decompression rates, from 0 to 100 kPa/s, were controlled by caps pierced with holes of different diameters and screwed onto the valve. Seven pressure sensors were sunk into the granular material and measured the air pressure P at different depths. An eighth sensor (sensor 1, Fig. 2b) measured the air pressure $P_s + P_{atm}$ above the particle bed. The pressure sensors were 86–005G–C (for sensors 1, 3, 5 and 8, Fig 2b) and 86–015G–C (for the others) of TE–Connectivity, with a maximal pressure range of 5 psi (~ 34 kPa) and 15 psi (~ 103 kPa) respectively and an accuracy of ~ 23 Pa and ~ 70 Pa. The sensors were recalibrated before each experiment with water levels in the vertical pipe to correct for potential instrumental drift. The measurements were taken at 1000 Hz. An LED lit up when acquisition was triggered to synchronize the measurements with the videos (25 Hz and 500 Hz). To make the bubbles more visible, some experiments were done with the box tilted slightly backwards to force the bubbles to move across the tank window.

Because the decompression rate is quasi exponential, it varies with time. For a comparison with the numerical results, the values given in the *Experimental Results* section are the mean value, $\bar{P}_s$ (defined as the point at which the air overpressure is half that of the initial overpressure). The maximal decompression rate ranges from the mean value itself (for the highest decompression rates) up to 3 times the mean value (for the lowest decompression rates). A total of 270 experiments were carried out using the glass beads, varying the slope of the tank and/or the granular bed (0, 2, 10, 15, 20°), the initial gas overpressure (from 5 to 30 kPa), the decompression rate (0 to 100 kPa/s), the bed thickness (15, 20, 25 cm) and the temperature

(20°C to 60°C). A total of 50 experiments were carried out using the ignimbrite (H=10 cm to H=20 cm, slopes from 0 to 30°, temperature from 20°C to 150°C).

Numerical model

The numerical model follows the development of ref[35] and is given in Code availability. We simplified the problem by assuming that the granular bed is non–expansive (as observed for slow decompression rates). Mass conservation of the gas implies that:

$$\frac{\partial}{\partial t}\left(\varepsilon\rho_g\right)+\frac{\partial}{\partial z}\left(\varepsilon\rho_g u_g\right)=0 \quad (1)$$

where t is time, ε the porosity of the granular bed, ρ_g is gas density, z the elevation and u_g the gas velocity in the pores. The velocity in the pores is related to the Darcy velocity u_D (i.e. the volumetric rate of flow per unit area) with:

$$u_g=\frac{u_D}{\varepsilon}=-\frac{K}{\varepsilon\mu}\left(\frac{\partial P}{\partial z}-\rho_g g\right) \quad (2)$$

where μ is the gas viscosity, K is the gas permeability in the granular bed and g is gravity. The link between the gas density ρ_g and its pressure P is deduced from the perfect gas law:

$$\rho_g=\rho_{atm}\frac{P}{P_{atm}} \quad (3)$$

with ρ_{atm} the density of the air (1.2 kg/m^3) at atmospheric pressure P_{atm} (101.3 kPa).

To reproduce the experiments, the initial overpressure $P_{s0}+P_{atm}$ was set for the whole deposit. Then, a decrease in surface pressure P_s+P_{atm} was imposed following the experimental measurements from sensor 1. The pressure evolution in the granular bed was calculated by solving equations 1, 2 and 3. We explored various values for the permeability K, constant or varying in time and space. Numerical results were then compared to the experimental results to estimate the value of K and its range of variation (Extended Data Fig. 1). For low decompression rates, the bed expansion was small (little variation in the volume of space between the grains) and the whole defluidisation process was simulated with a constant value of K (2×10^{-12} m^2 for glass beads and 3×10^{-12} m^2 for the ignimbrite). For higher decompression rates, which induce fluidisation, the model showed that although the permeability varied in time and space, it remained within a relatively small range of values (e.g. between 2 and 4×10^{-12} m² for most experiments with glass beads, Fig. 4) except for the highest decompression rates with a large pressure gradient and bubbles, where K sometimes temporarily reached more than 10^{-11} m².
To predict if the granular material remains stable or if it flows, we calculated the apparent friction angle φ. A granular material can be stable on a slope due to friction between its constituent particles. This is described by a mechanical property called the friction angle. The friction angle δ of the material used is 27°±0.5° for the glass beads and 36°±0.5° for ignimbrite. The pressure gradient of the gas, by partially or totally sustaining the weight of the particles, lowers the friction and the apparent friction angle φ is given by:

$$\tan\varphi=\left(1-\frac{P-\left(P_s+P_{atm}\right)}{\rho g h}\right)\tan\delta \quad (4)$$

where P is the air pressure at depth h, P_s is the air overpressure at the bed surface (and at the base of the PDC) that decreases from P_{s0} to 0, g is gravity and ρ the mean density of the granular bed. With no gas pressure gradient, $\varphi=\delta$. This means that for slopes α of the bed surface lower than φ, non–cohesive material is stable. Above this value ($\alpha>\varphi$), it flows until stability is reached. The bed is fully fluidised above the depth h when the air pressure P rises sufficiently to create a value of $P-\left(P_s+P_{atm}\right)$ that is equal to the pressure of the particles above, so that φ equals 0. The bed flows like a fluid in a slope.

Fig. 4a, has been compiled using the results of 5000 simulations (shown in Extended Data Fig. 2), either by varying the parameters controlling the defluidisation (P_{s0}, H, ρ, K, μ, Δt) or by choosing sets of parameters, automatically and randomly, that give the imposed values of Π_1 and Π_2. We applied ranges of values characteristic of natural deposits for various parameters: permeability (K=10^{-13} to 10^{-10} m²), gas viscosity (μ = 1.85 at 20°C and 4.5×10^{-5} at 950°C), deposit thickness (H =10 cm to 10 m), deposit density (ρ from 500 to 2000 kg/m^3), unloading times (Δt from 0 to 300 s) and basal overpressures of PDC (P_{s0} from 1 to 100 kPa). The surface overpressure P_s decreases linearly from P_{s0} to 0 (Fig. 4b). The maximal depth of fluidisation H_f, for φ=0 and φ=10° and the time of fluidisation of the upper 10 centimetres are then used to calculate H_f/H and $t_{f10}/\Delta t$. $\bar{P}_s$, in the definition of Π_2, is the mean value of the gas pressure at the base of the PDC and acts on the defluidisation by changing the gas density through its compressibility β. It is approximated by $\bar{P}_s = P_{atm} + P_{s0}/2$ but because the gas pressure in the deposit changes in time and space in a non–linear way, this approximation induces an error in the prediction of H_f/H of up to 20% for low thicknesses (Π_2<1) and between simulations done at high and low pressure (see Extended Data Fig. 2).

Data availability

Videos and synchronized pressure data (text files) of characteristic experiments can be downloaded here: https://doi.org/10.25519/TF5A-8291

Code availability

The numerical code used (open source) is available here: https://doi.org/10.25519/TF5A-8291

The estimation of the pressure and the decompression rate in the field has been done with the version "Pyroclastic flows and surges" of VolcFlow downloadable here: https://lmv.uca.fr/volcflow/

Corresponding author

Correspondence to Karim Kelfoun (karim.kelfoun@uca.fr)

Extended data:

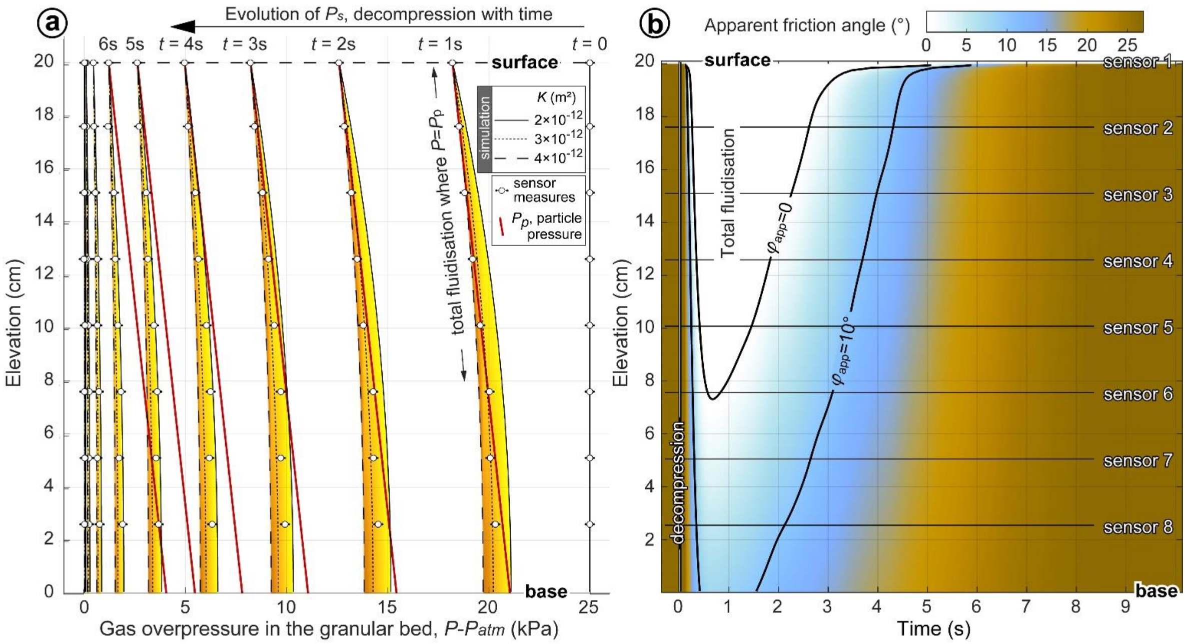

Extended data Figure 1: Numerical simulation of one laboratory experiment. (a) Pressure evolution in the deposit for $K = 2\times10^{-12}$, 3×10^{-12} and 4×10^{-12} m². The experimental measurements are given by the white circles. Where the particle pressure is equal to or lower than the gas pressure, the granular material is fully fluidised locally. (b) Evolution of the apparent friction angle δ with time for $K = 3\times10^{-12}$ m². During decompression, the flow is fully fluidised down to about 12 cm beneath the surface and the apparent friction angle of less than 10° shows that all the material can flow on steeper slopes for more than 1 s (and the upper surface for 4 s). Because the geometry change induced by the flow was not simulated, results are compared with experiments carried out on the horizontal but the time of fluidisation coincides with the flow duration of experiments carried out on a slope and in the same conditions.

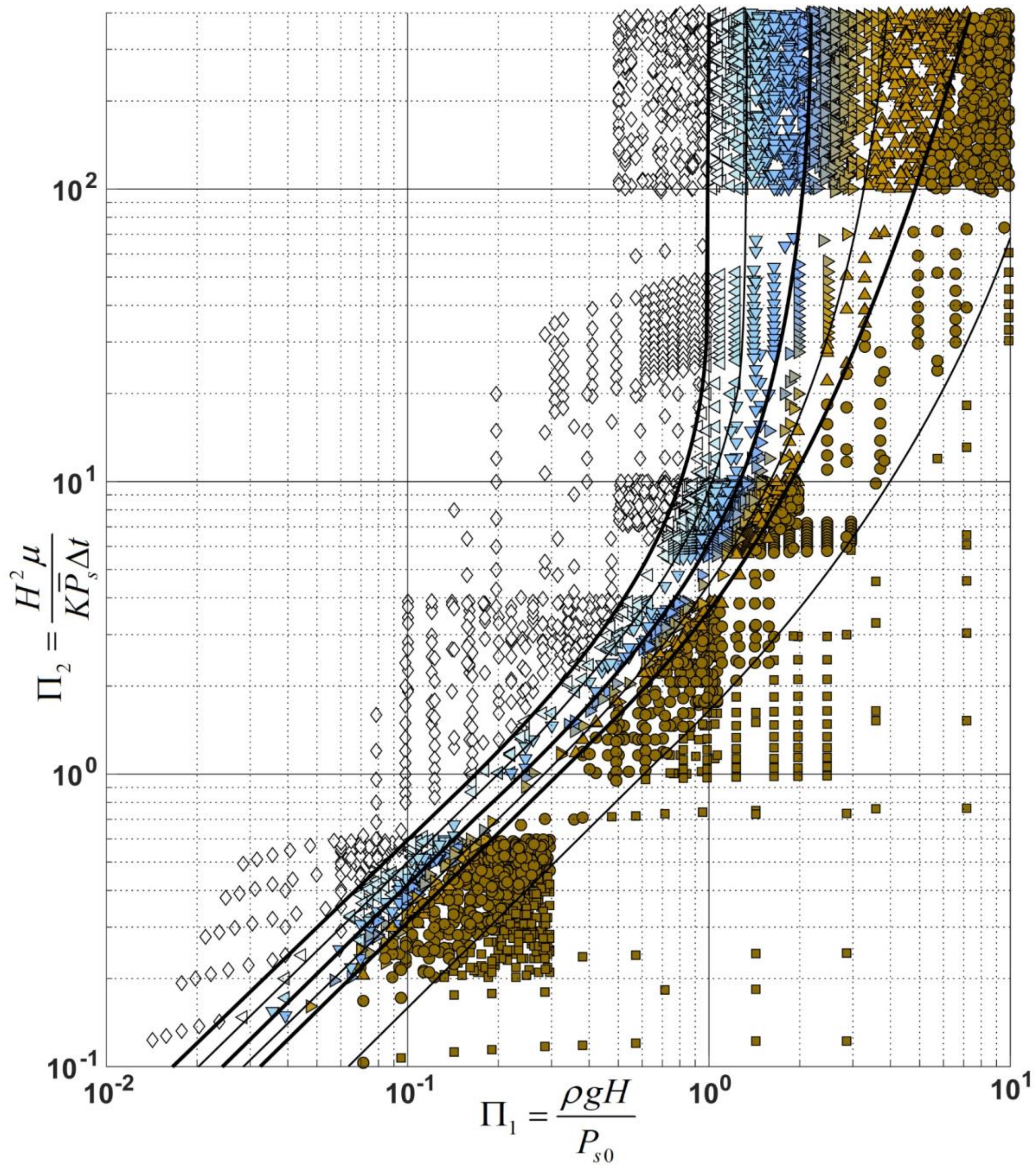

Extended data Figure 2: Evolution of the ratio H_f/H according to Π_1 and Π_2. The colours give the values of H_f/H of each of the 5000 simulations used to draw the curves (some points overlap exactly). The data used to make the figure are available here: https://doi.org/10.25519/TF5A-8291. They have been made with the numerical code available in the same repository.